Apical annuli are specialised sites of post-invasion secretion of dense granules in *Toxoplasma*

Sara Chelaghma[1†], Huiling Ke[1†], Konstantin Barylyuk[1], Thomas Krueger[1], Ludek Koreny[1*] and Ross F. Waller[1*]

[1] Department of Biochemistry, University of Cambridge, Cambridge, CB2 1QW, UK
[†] Equal contribution
* Correspondence: Ludek Koreny, lk360@cam.ac.uk; Ross F Waller, rfw26@cam.ac.uk

Abstract

Apicomplexans are ubiquitous intracellular parasites of animals. These parasites use a programmed sequence of secretory events to find, invade, and then reengineer their host cells to enable parasite growth and proliferation. The secretory organelles micronemes and rhoptries mediate the first steps of invasion. Both secrete their contents through the apical complex which provides an apical opening in the parasite's elaborate inner membrane complex (IMC) — an extensive subpellicular system of flattened membrane cisternae and proteinaceous meshwork that otherwise limits access of the cytoplasm to the plasma membrane for material exchange with the cell exterior. After invasion, a second secretion programme drives host cell remodelling and occurs from dense granules. The site(s) of dense granule exocytosis, however, has been unknown. In *Toxoplasma gondii*, small subapical annular structures that are embedded in the IMC have been observed, but the role or significance of these apical annuli to plasma membrane function has also been unknown. Here, we determined that integral membrane proteins of the plasma membrane occur specifically at these apical annular sites, that these proteins include SNARE proteins, and that the apical annuli are sites of vesicle fusion and exocytosis. Specifically, we show that dense granules require these structures for the secretion of their cargo proteins. When secretion is perturbed at the apical annuli, parasite growth is arrested. The apical annuli, therefore, represent a second structure in the IMC specialised for protein secretion, and reveal that in *Toxoplasma* there is a physical separation of the processes of pre- and post-invasion secretion that mediate host-parasite interactions.

Keywords: *exocytosis, dense granule, apical annuli, inner membrane complex, SNARE proteins, Toxoplasma, Apicomplexa*

Introduction

Apicomplexa is a phylum of ubiquitous eukaryotic parasites of animals of broad medical, veterinary, and ecological importance. In humans they are responsible for diseases such as malaria, cryptosporidiosis and toxoplasmosis causing wide-spread mortality and morbidity which disproportionately affects developing world regions (Havelaar et al., 2015; Montoya and Liesenfeld, 2004; Striepen, 2013; WHO, 2021). Commercial live-stock industries and subsistence farming also suffer heavy losses from diseases caused by apicomplexans, including coccidiosis in poultry, babesiosis and theileriosis in cattle, and fetal death in sheep and goats from toxoplasmosis (MacGregor et al., 2021). Apicomplexans belong to a larger group of related unicellular eukaryotes including ecologically important dinoflagellates and ciliates that together form the supergroup Alveolata. Common to these organisms is a complex cell pellicle derived from a tessellation of flattened membrane alveolar vesicles appressed to the inner face of the

cell's plasma membrane and supported by a complex proteinaceous membrane skeleton (Anderson-White et al., 2012; Gould et al., 2008). This cell pellicle provides broad structural and functional roles to these cells. In apicomplexans the pellicle defines their distinctive cell shape and provides a platform for both gliding motility machinery and signalling networks, all of which are critical to the parasites' ability to navigate their animal host tissues and invade selected cells.

A common challenge posed to alveolate cells by their complex pellicle is that it limits opportunities for material exchange across the plasma membrane. The alveolar vesicles and subpellicular proteinaceous networks, collectively called the Inner Membrane Complex (IMC) in apicomplexans, typically line most of the inner cell surface. Dedicated structures within the IMC are, therefore, required to provide access to the plasma membrane for processes such as exocytosis and endocytosis. In apicomplexans an apical complex is one such structure that provides an apical opening in the IMC to allow exocytosis from two invasion-related organelles: micronemes and rhoptries (Koreny et al., 2021; Pacheco et al., 2020). Secretion of microneme proteins promotes parasite egress from its host cell, gliding motility, and then apical contact with its next host cell to invade. At this point, secretion from rhoptries facilitates host cell entry and some countering of the host cell's immune response (Hakimi et al., 2017). The apical complex is composed of an apical polar ring of proteins, that excludes the IMC, and within which sits a hollow tubulin-based conoid. The micronemes and rhoptries extend through the conoid to reach the free plasma membrane at this apical site. The requirement for microneme and rhoptry secretion for invasion makes this an essential structure to these parasites. A second dedicated type of structure in the IMC allows material transfer in the opposite direction. Micropores are small invaginations of the plasma membrane that are supported by a collar of proteins positioned at the intersections of IMC alveolar vesicles (Nichols et al., 1994). While these structures were first observed in early electron microscopy on these cells, their role in endocytosis has been only recently established (Koreny et al., 2023; Wan et al., 2023). Both the apical complex and micropores are found throughout apicomplexans, as well as in related dinoflagellates, perkinsids and chrompodelids, which suggests that they have been fundamental features of the evolution of the complex pellicle of Alveolata.

A third, enigmatic type of annular structure has been observed within the IMC of the apicomplexan *Toxoplasma gondii*. This structure occurs as a series of ~5-8 small annuli in a ring around the periphery of the cell but towards its apical end (Engelberg et al., 2020; Hu et al., 2006). Originally named peripheral annuli, but now more commonly called apical annuli, these structures were previously known only from protein location patterns as rings but were otherwise cryptic in ultrastructural studies. Electron microscopy on shadow-cast detergent extractions of *T. gondii* pellicles, however, do reveal small rings, intercalated between the subpellicular network of microtubules at the expected position for the apical annuli (Díaz-Martin et al., 2022). The proteins initially characterised at the apical annuli lacked membrane-binding domains and appeared to interact with proteins of the IMC sub-pellicular network including 'suture' proteins that occur where alveolar vesicles are sealed together (Engelberg et al., 2020; Hu et al., 2006; Suvorova et al., 2015). This implied that the apical annuli were features of the IMC occurring at alveolar junctions, but it was not known if these structures interacted with or were relevant to the plasma membrane or cell surface. Mutations of proteins specific to the apical annuli lacked clear phenotypes that could inform on the significance or function of these structures (Engelberg et al., 2020). Therefore, it has been a mystery what the apical annuli might do in these cells.

A second conundrum of the apicomplexan pellicle has been where does the third major class of exocytic vesicles, the so-called dense granules, exocytose from the cell? Dense granule proteins are secreted after the parasite has invaded its new host (Carruthers and Sibley, 1997). They

deliver a complex mixture of proteins that establish the parasitophorous vacuole in which the parasite resides in its host, and also target a wide range of host cell organelles to reengineer this environment in which it grows (Griffith et al., 2022; Lebrun et al., 2014). These functions includes interfering with host signalling networks and transcriptional programmes that would otherwise seek to attack the intruder (Hakimi et al., 2017). The identification of dense granule organelles throughout Apicomplexa is more challenging because they lack the conspicuous morphologies that characterise micronemes and rhoptries, and they tend to have fast-evolving and unique protein repertoires specific to each parasite-host interaction (Barylyuk et al., 2020; Guérin et al., 2023). Nevertheless, it is presumed that most apicomplexans rely on equivalent post-invasion secretion. Dense granules also differ from micronemes and rhoptries, which are permanently concentrated around the cell apex, in that they are dispersed throughout the cell. They are highly motile on cytoskeletal networks, and they have been seen to accumulate towards the apex during invasion events (Heaslip et al., 2016; Venugopal et al., 2020). While some evidence of their secretion from the apical region of the cell has been proffered, the precise sites or mechanism of dense granule exocytosis has remained unknown (Dubremetz et al., 1993).

In our study we have asked if any specific plasma membrane proteins occur at the apical annuli sites in *T. gondii* and, if so, could these inform on apical annuli function including the processes of post-invasion dense granule protein secretion?

Results

The apical annuli structures span the parasite plasma membrane

The question of whether the apical annuli structures of *Toxoplasma gondii* extend to include the plasma membrane was fortuitously answered by our independent investigations of *T. gondii* membrane proteins at the cell surface. During the verification of protein location assignments from our hyperLOPIT spatial proteomic studies, we C-terminally reporter tagged an uncharacterised protein (TGME49_222200) that was assigned as a transmembrane protein of the plasma membrane by hyperLOPIT (Barylyuk et al., 2020). By immuno-fluorescence assay (IFA) the endogenously reporter-tagged TGME49_222200 showed a distinctive surface location pattern of ~5-8 puncta arranged as a subapical ring at the cell surface (Fig 1A). Centrin2 is a known marker of the apical annuli, although it additionally occurs at discrete locations at the conoid, centrosome and basal complex (Hu et al., 2006; Leung et al., 2019). TGME49_222200 was exclusively located to the Centrin2 apical annuli positions (Fig 1A). The predicted membrane topology of this new protein includes nine transmembrane domains with a cytosolic C-terminal extension (Fig 1B). To verify the plasma membrane location of this protein we performed trypsin proteolytic shaving of live parasites. TGME49_222200, which migrates as a double band, showed rapid trypsin sensitivity (Fig 2C). Similarly, the surface protein SAG1 was progressively diminished as internal SAG1 pools recycled to the surface (Gras et al., 2019; Koreny et al., 2023), whereas internal marker proteins (GAP40, PRF, TOM40) were all trypsin-protected by the plasma membrane. These data are consistent with exposure of inter-transmembrane loops of TGME49_222200 at the cell surface and, therefore, that the apical annuli are structures that extend to the surface environment of the cell.

Can this new plasma membrane protein inform us of apical annuli function? TGME49_222200 contains a conserved Limb Development Membrane Protein 1 domain (LMBD) that consists of 9 trans-membrane helices in a 5+4 arrangement (Fig 1B) but whose functions are generally not well studied (Redl and Habeler, 2022). Furthermore, multiple paraloguous LMBD proteins exist in

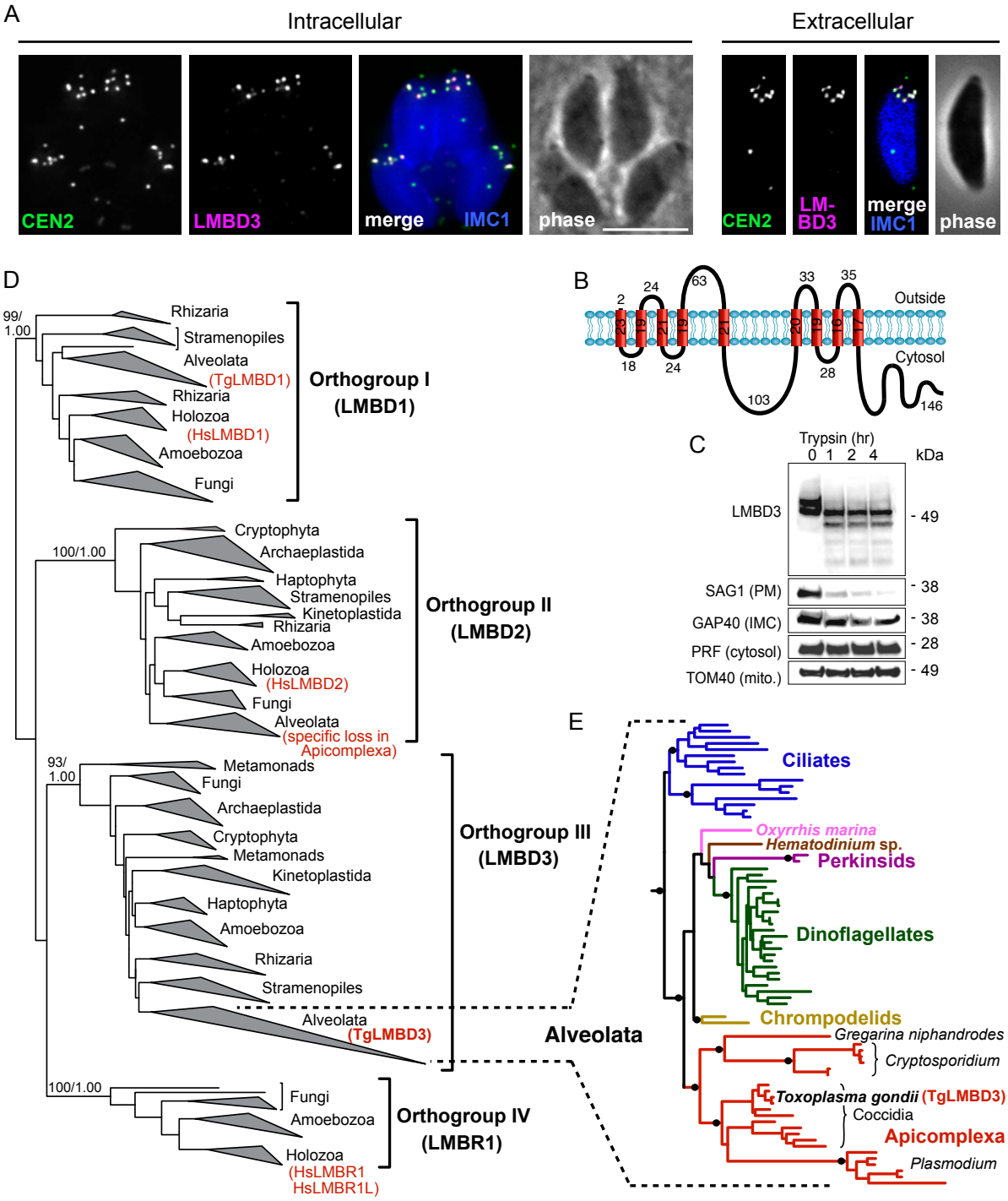

Figure 1: *Tg*LMBD3 is a conserved protein in the plasma membrane at apical annuli sites in *T. gondii*. (A) Wide-field immuno-fluorescence assay imaging of cells expressing *Tg*LMBD3-6xHA (magenta) and eGFP-Centrin2 (green) and immuno-stained IMC1 (blue) in either the intracellular stage in hosts or extracellular tachyzoites. Scale bar = 5 µm. (B) Membrane topology of *Tg*LMBD3 by DeepTMHMM (Hallgren et al., 2022) with numbers indicating amino acid domain lengths. (C) Trypsin-shaving sensitivity over four hours (hr), visualised on Western blots, of *Tg*LMBD3-6xHA and markers of the exterior leaflet of the plasma membrane (PM), IMC, cytosol (PRF, profilin) and mitochondrion (mito.). kDa, kilodalton. (D) Maximum likelihood phylogeny of LMBD proteins resolving as four major orthogroup clades. Node support values are bootstraps followed by aLRT SH-like supports. (E) Expanded Alveolata clade from LMBD Orthogroup III showing major groups. Black dots indicate aLRT SH-like support >0.95. See Fig S1 for full phylogenies.

eukaryotes, so we first asked if TGME49_222200 belonged to an orthogroup with any functional characterisation. A global phylogeny of LMBD proteins shows that four LMBD orthogroups exist (Fig 1D, Fig S1A). TGME49_222200 belongs to orthogroup III and, hence, we refer to this protein as *Tg*LMBD3 hereafter. Although orthogroup III is widely present in eukaryotes, all animals (holozoa) have lost this paralogue, and none have been functionally characterised. Nevertheless, orthologues of *Tg*LMBD3 are retained in all apicomplexans, and throughout their close alveolate relatives (including dinoflagellates and ciliates) (Fig 1E, Fig S1B). Thus, while a function for *Tg*LMBD3 cannot be readily identified from orthologues, its strong conservation throughout Apicomplexa implies that it performs an important function in *Toxoplasma*.

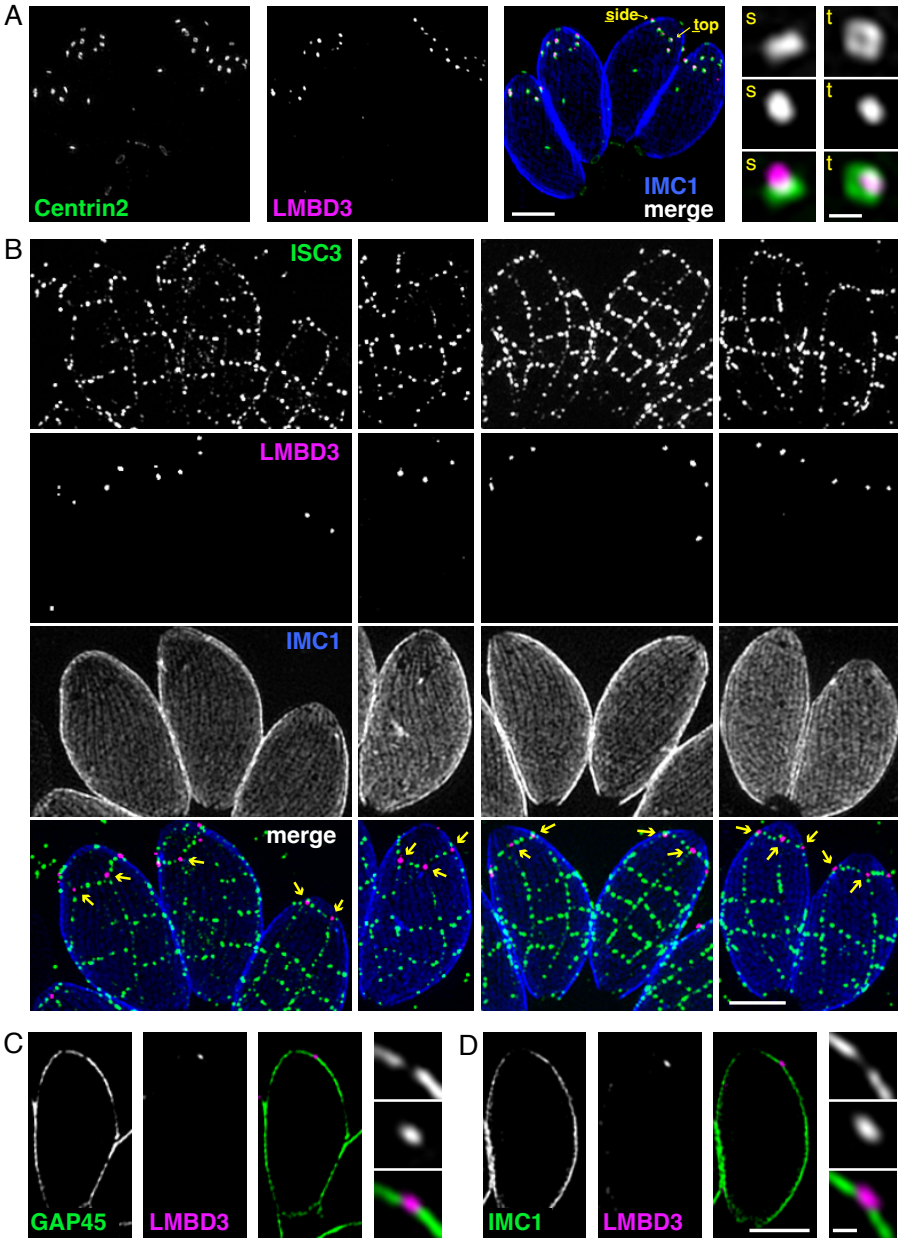

Figure 2: Apical annuli occur at gaps in the IMC. 3D-SIM imaging of immuno-fluorescence assays of intracellular tachyzoites in host cells. (A) *Tg*LMBD3-6xHA (magenta) and eGFP-Centrin2 (green) expressing cells with side (s) and top (t) projections of apical annuli shown in zoom. IMC1 (blue). (B) Suture protein ISC3-3xV5 (green) co-expressed with *Tg*LMBD3-6xHA (magenta) showing apical annuli positioned at the apical cap suture where it intersects with longitudinal sutures (arrows). IMC1 (blue). (C, D) Optical sections showing GAP45 or IMC1 (green) with *Tg*LMBD3-6xHA (magenta) showing gaps in these IMC proteins where apical annuli occur. All scale bars = 2 µm or 200 nm for zoomed panels.

183 **Apical annuli occur at gaps in the IMC and potential plasma membrane access**

184 Given that *Tg*LMBD3 implicates the plasma membrane in apical annuli function, we asked if the
185 IMC is coordinated with the apical annuli sites to allow interaction here between the plasma
186 membrane and the rest of the cell cytosol? We first sought higher resolution position information
187 for *Tg*LMBD3 relative to the small rings that Centrin2 delineates. Three-dimensional structured
188 illumination microscopy (3D-SIM) resolved *Tg*LMBD3 as a small punctum within the Centrin2
189 rings although slightly peripheral to it, consistent with *Tg*LMBD3 being in the plasma membrane
190 and Centrin2 associated with the IMC beneath (Fig 2A). We then asked how *Tg*LMBD3 is
191 positioned with respect to the IMC cisternae boundaries by staining the IMC suture protein ISC3
192 (Chen et al., 2017). The *Tg*LMBD3-labelled annuli were always positioned at the cisternae
193 boundaries, specifically where the apical cap boundary intersects with the longitudinal suture
194 boundaries (Fig 2B). All such intersections observed contained a *Tg*LMBD3 punctum and,
195 hence, the variable number of apical annuli from cell to cell is apparently defined by the number
196 of longitudinal IMC boundaries. The IMC is supported on its plasma membrane-facing surface by
197 GAP45, and on its cytosol-facing surface by IMC1 (Anderson-White et al., 2011). While both
198 proteins occur throughout the peripheral IMC regions of the cell, both showed an interruption
199 where the *Tg*LMBD3 puncta occur (Fig 2C and D). Centrin2, and other markers of the apical
200 annuli, are recruited to the IMC during early stages of daughter cell formation (Engelberg et al.,
201 2020). In apicomplexans, these early cell stages lack the plasma membrane which is only
202 recruited when the new cells emerge from within the mother cell — the process of endodyogeny
203 in *Toxoplasma*. Given that *Tg*LMBD3 is a plasma membrane protein, we asked when is this
204 protein recruited to the apical annuli? Cells captured throughout the process of endodyogeny
205

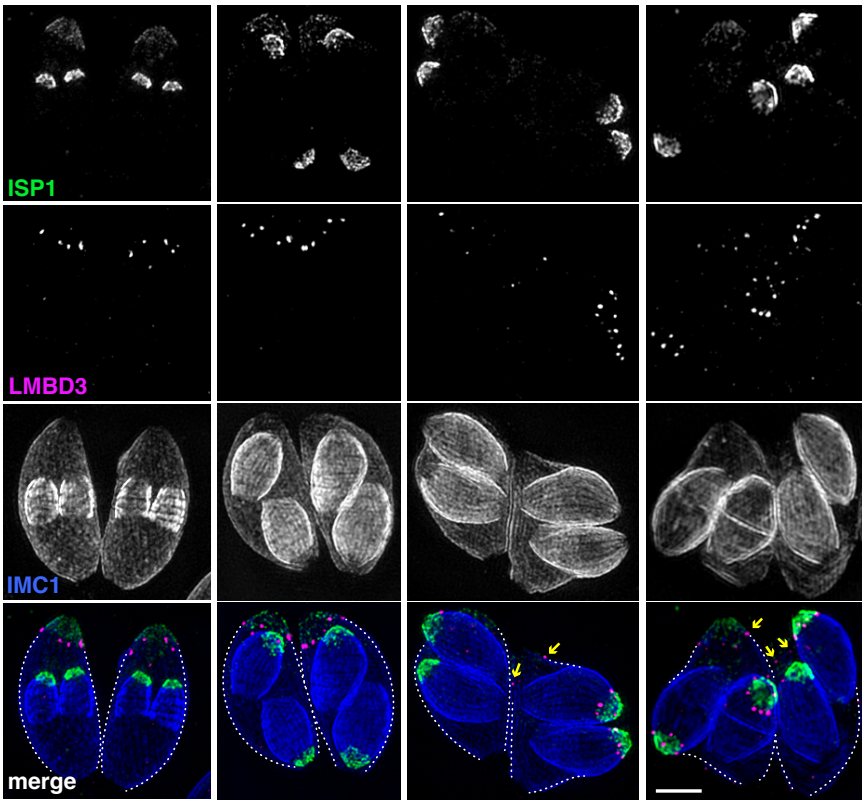

206
207
208 **Figure 3: *Tg*LMBD3 is recruited to the apical annuli late in cytokinesis.** 3D-SIM imaging of immuno-
209 fluorescence assays of intracellular tachyzoites at various stages of daughter cell formation and emergence from
210 the mother cell. Maternal annuli are indicated with arrows. *Tg*LMBD3-6xHA (magenta) co-labelled with apical cap
211 marker ISP1 (green) and IMC1 (blue). Scale bar = 2 µm.

212 showed that *Tg*LMBD3 only appears at apical puncta as the cell apex emerges from the mother
213 cell at the time of plasma membrane recruitment (Fig 3). Relicts of the mother cell's apical annuli
214 *Tg*LMBD3 persist at this stage (Fig 3, arrows) suggesting that little or no *Tg*LMBD3 is recycled
215 from mother to daughter. Collectively these data imply that the apical annuli provide coordinated
216 gaps in the IMC barrier that forms at the earliest point of IMC development and that they
217 maintain access of the cytosol to these specialised locations in the plasma membrane.
218

219 **Apical annuli recruit SNARE proteins**

220 Because *Tg*LMBD3 did not provide an obvious clue to why the plasma membrane should be
221 accessible at the apical annuli, we asked if there are other plasma membrane-associated
222 proteins at these sites. We employed a proximity-dependant biotinylation approach (BioID) using
223 *Tg*LMBD3 as a promiscuous biotin ligase (BirA*)-conjugated bait. This approach recovered
224 known apical annuli proteins as the most significantly BioID-enriched proteins (e.g., AAP2-5,
225 Table S1). However, in pursuit of plasma membrane-associated proteins, we looked for any
226 detected biotinylated proteins with hyperLOPIT location assignments as integral plasma
227

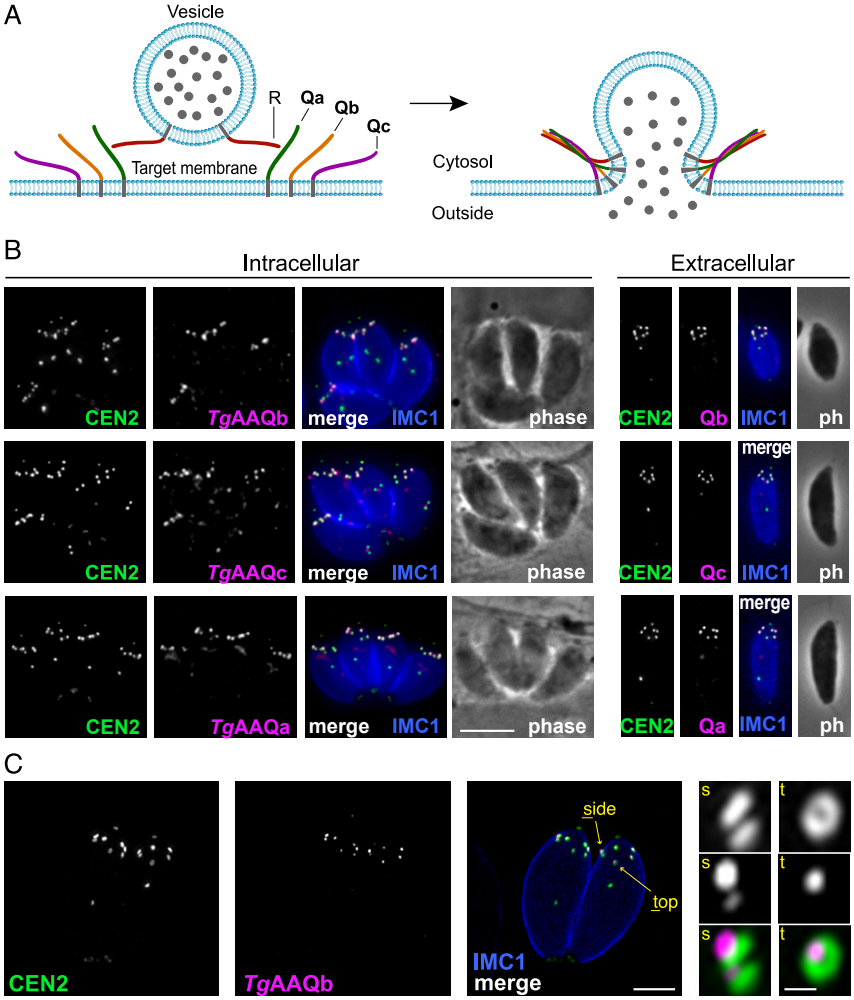

228
229

230 **Figure 4: Three SNARE proteins likely form a complex at the inner side of the plasma membrane at the**
231 **apical annuli.** (A) Schematic of the SNARE complex which facilitates fusion of a secretory vesicle with target
232 membrane. (B) Wide-field fluorescence microscopy localization of *Tg*AAQa, *Tg*AAQb and *Tg*AAQc SNAREs
233 expressed in *T. gondii* (as mAID-3xV5 N-terminal fusions) and co-stained for eGFP-Centrin2. All panels are in
234 the same magnification with scale bar = 5 µm. (C) 3D-SIM microscopy image of *Tg*AAQb with Centrin2. The
235 zoomed panels show the apical annuli either in side (s) or top (t) projection as indicated. The scale bars for large
236 and small (zoomed) panels are 2 µm and 200 nm, respectively.

membrane proteins (Table S1) (Barylyuk et al., 2020). Amongst these proteins were three SNARE (Soluble N-ethylmaleimide-sensitive factor attachment protein receptor) proteins, each containing either a Qa SNARE domain (TgME49_209820), Qb SNARE domain (TGME49_306640) or Qc SNARE domain (TGME49_253360). These three domain-containing proteins typically function at a target membrane of vesicle fusion by forming heterotetrameric complexes with a vesicle-bound R SNARE which drives the fusion of the vesicle (Fig 4A). To test if the three Q SNAREs occur at the apical annuli, each protein was endogenously N-terminally reporter-tagged (C-terminal fusions are not tolerated by these tail-anchored membrane proteins) and their locations visualised by IFA. All three SNAREs showed distinct apical annuli locations (Fig 4B). The Qb SNARE is exclusively located at apical annuli, whereas the Qa and Qc SNAREs show some additional signal as a single structure in the central region of the cell (Fig 4B). Super resolution imaging of the Qb SNARE shows a similar location to *Tg*LMBD3 relative to Centrin2: a small punctum centred on the Centrin2 ring but displaced towards the plasma membrane (Fig 4C). We designate these three SNAREs *Tg*AAQa, *Tg*AAQb and *Tg*AAQc (Apical Annuli Qa, Qb, Qc) based on their locations at the apical annuli. Together, these SNAREs implicate the annuli as sites for exocytic vesicle fusion at the plasma membrane.

Apical annuli provide essential function for normal cell growth

Mutations of previously identified apical annuli proteins have shown either no phenotype, or phenotypes that could not be discerned from possible additional functions of proteins, such as Centrin2 that occur at non-apical annuli cell sites also (Engelberg et al., 2020; Lentini et al., 2019; Leung et al., 2019). So, the importance of these cell structures to cell fitness was unknown. Using the four plasma membrane-associated apical annuli proteins we asked if these structures are required for typical cell growth. We made auxin-inducible degron (AID) knockdown cell lines (using the mini (m) AID peptide) for the four proteins: *Tg*LMBD-mAID-3xV5), mAID-

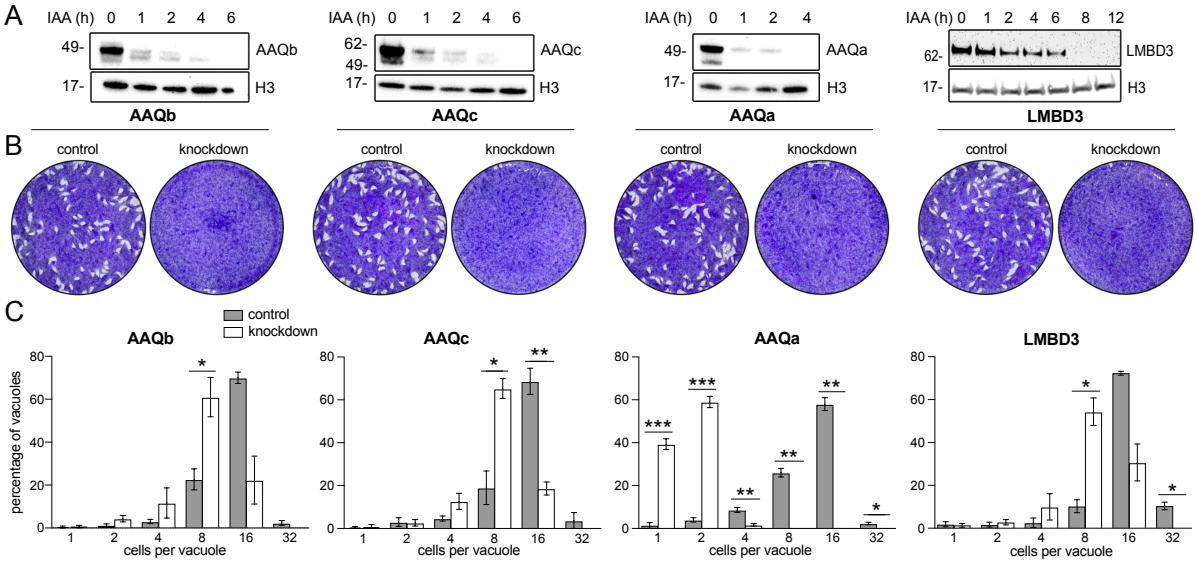

Figure 5: Depletion of apical annuli plasma membrane proteins impairs replication rates of *T. gondii*. (A) Depletion of each apical annuli protein show in hours of 3-indolacetic acid (IAA) auxin treatment observed by anti-V5 Western blots. Histone H3 serves as a loading control, and molecular weight markers in kDa are shown. (B) Plaque assays in host cell monolayers showing plaque development over 8 days in knockdown cell lines for each apical annuli protein without (control) or with IAA-induced protein knockdown. (C) Replication states of *T. gondii* parasitophorous vacuoles 24 hours post invasion scored according to parasite number per vacuole. Each protein knockdown cell line is assayed either without (control) or with IAA-induced protein knockdown. Significant statistical differences between vacuole types are indicated by p-values * <0.05; ** <0.01; *** <0.001.

273 3xV5-*Tg*AAQa, mAID-3V5-*Tg*AAQb and mAID-3xV5-*Tg*AAQc, and tested for growth phenotypes.
274 All proteins were depleted to undetectable levels within 3-12 hours of auxin (3-indolacetic acid)
275 treatment (Fig 5A). Plaque assays assess tachyzoite competence for the entire lytic cycle, and
276 the depletion of all four proteins showed strong phenotypes of reduced plaque development (Fig
277 5B). We then tested specifically for effects of each protein knockdown on parasite replication
278 within the host cell. Depletion of all proteins resulted in delayed parasite replication at 24 hours
279 post invasion (Fig 5C). All mutants showed an average lag of one to three division cycles behind
280 the control, with the depletion of *Tg*AAQa showing the most severe retardation of parasite
281 replication. These data show that the apical annuli are necessary for cell proliferation in the host
282 cell environment.
283
284 **Apical annuli are required for dense granule exocytosis**

285 Micronemes and rhoptries release their contents during the initial events of host cell invasion by
286 fusing with the plasma membrane accessed through the conoid at the cell's apex (Aquilini et al.,
287 2021; Dubois and Soldati-Favre, 2019). Dense granule contents, however, are secreted post
288 invasion and the site of their release from the parasite has been unknown. Our data for SNARE
289 proteins at the apical annuli offers these locations as possible points for dense granule docking
290 and exocytosis. To test if dense granule protein secretion is perturbed when either the *Tg*AAQ
291 SNAREs or *Tg*LMBD3 are depleted we assayed for GRA1, GRA2 and GRA5 secretion in our
292 knockdown cell lines. Secreted GRA5 is delivered to the parasitophorous vacuolar membrane.
293 IFAs for GRA5 were performed with digitonin cell permeabilization that results in only limited
294 disruption of the parasite plasma membrane. This enabled the secreted GRA5 to be
295 preferentially detected (non-secreted GRAs will additionally occur in dense granules within the
296 parasites). All four protein knockdowns showed reduced GRA5 delivered to the parasitophorous
297 vacuole membrane (Fig 6A). GRA1 and GRA2 are secreted into the parasitophorous vacuole
298 space and upon fixation for IFAs both proteins typically show regions of accumulated signal
299 between the parasites (Fig 6B and C, arrows). Depletion of *Tg*AAQb and *Tg*AAQc showed clear
300 reductions in this secreted signal (Fig 6B and C). When *Tg*LMBD3 was depleted a reduction in
301 GRA1/2 secretion was less evident, and *Tg*AAQa depletion retarded vacuole development to the
302 two-cell vacuole stages making visualisation of these secretion signals more difficult.
303
304 Non-secreted GRAs inside the parasites were evident in the GRA1/2 IFAs where TritonX-100
305 permeabilization enabled antibody access to the dense granules. When the secreted GRA1/2
306 signal was reduced upon apical annuli protein knockdown, the GRA signal seen within the
307 parasite was increased compared to the control (Fig 6B and C). By comparison, no change was
308 seen in either microneme or rhoptry number, morphology, or staining intensity when any of the
309 four proteins were depleted (Fig S2). Hence, this elevation in dense granule number with apical
310 annuli disruption is specific to this class of exocytic compartments.
311
312 Given the IFA evidence for both reduced secretion of three GRAs and accumulation of dense
313 granules within the parasites when apical annuli function was perturbed, we asked what other
314 proteins are elevated within the parasite in these conditions? We predicted that many GRAs
315 would show increased abundance in the parasite if dense granule exocytosis was inhibited. To
316 address this question, we performed quantitative shotgun proteomics on whole parasites grown
317 in host cells for 24 hours with or without auxin treatment for three cell lines: *Tg*LMBD-mAID-
318 3xV5, mAID-3xV5-*Tg*AAQb and mAID-3xV5-*Tg*AAQc (mAID-3xV5-*Tg*AAQa was excluded from
319 this analysis because of the risk of secondary effects of the severe growth phenotype with
320 *Tg*AAQa depletion, and the challenge of harvesting adequate cell material from these poorly
321 replicating cells). Protein abundance changes were visualised as volcano plots (Fig 6A). For all

three apical annuli protein depletions, dense granule proteins overwhelmingly dominated the proteins of increased abundance in the cells. For *Tg*LMBD3 depletion, the GRAs were almost exclusively the proteins whose increase was significant. Even the changes in GRA abundances that were assessed as non-significant in all three knockdowns at this timepoint were strongly skewed towards being increased. These data provide further strong evidence that perturbation of apical annuli function results in reduced secretion of dense granule proteins.

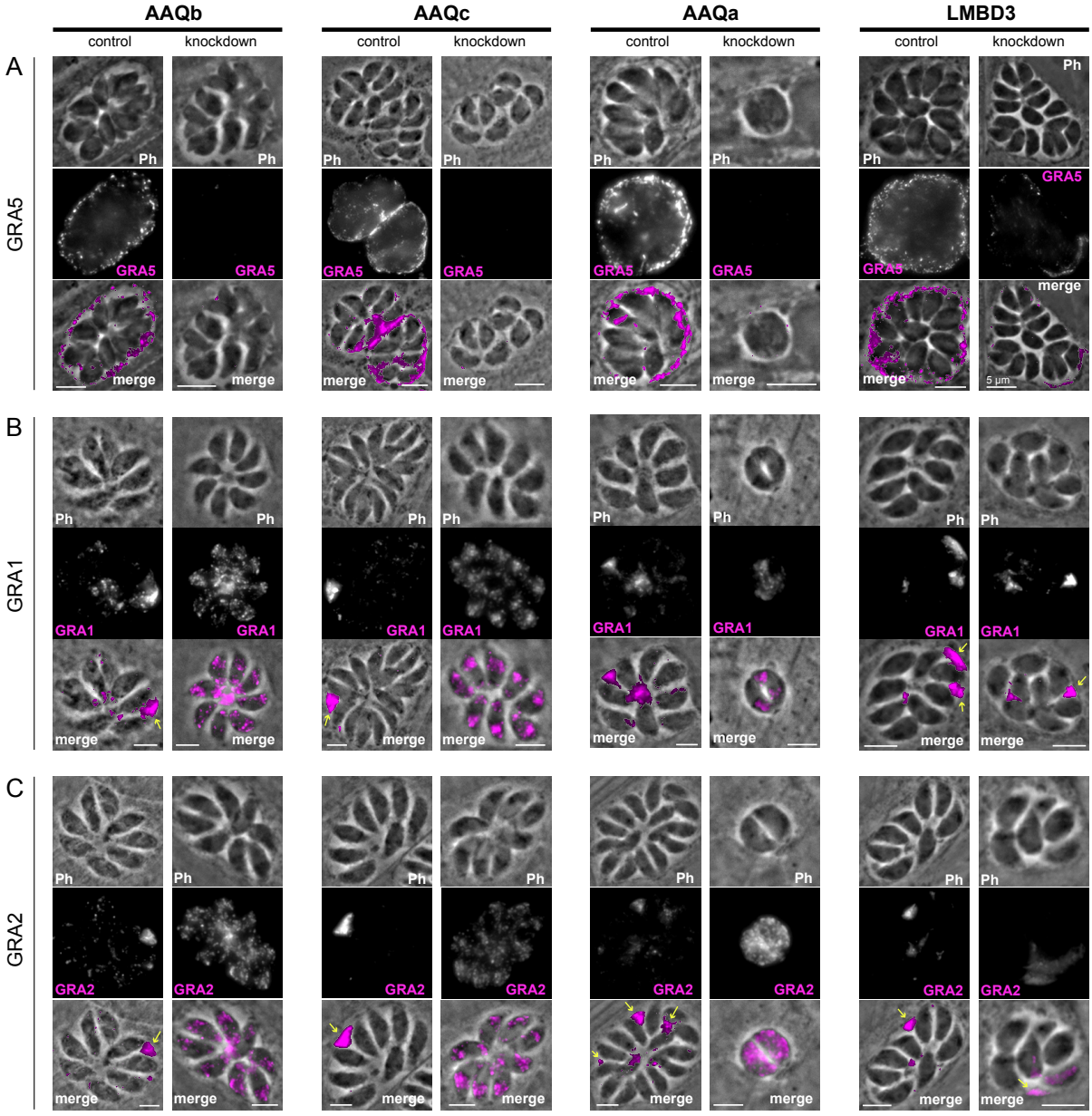

Figure 6: Secretion of dense granule proteins into the parasitophorous vacuole is inhibited when apical annuli membrane proteins are knocked down. Wide-field immuno-fluorescence assays of (A) GRA5, (B) GRA1 and (C) GRA2 without (control) or with auxin-induced protein knockdown for the four apical annuli membrane proteins. Assays for GRA5 were performed using digitonin permeabilization to preferentially stain the secreted protein only. Assays for GRA1 and GRA2 were performed with TritonX-100 permeabilization to visualise the non-secreted dense granules as well as the secreted GRAs. Scale bar = 5 µm.

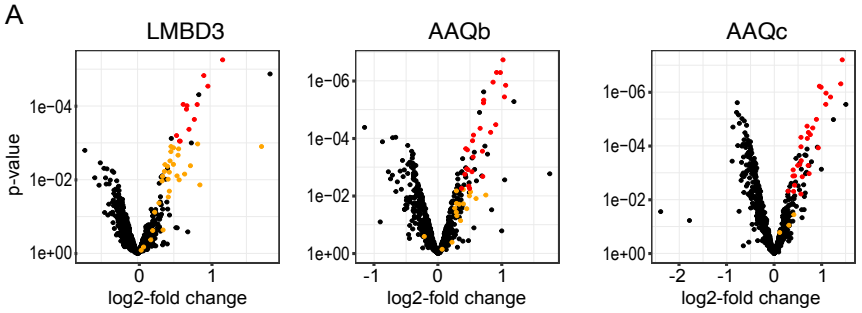

B

LMBD3

protein nb.	adj. p-value	FC
(1) 224460	0.004	3.55
(2) 203600	0.004	2.25
(3) 275440	0.004	1.88
(4) 237880	0.006	1.96
(5) 244280	0.008	1.80
(6) 277270	0.010	1.77
(7) 227620	0.010	1.60
(8) 251540	0.010	1.55
(9) 227280	0.011	1.60
(10) 270240	0.019	1.72
(11) 319340	0.032	1.63
(12) 220950	0.043	1.45
(13) 215980	0.048	1.38
(14) 212300	0.049	1.50
(15) 203310	0.049	1.49

AAQb

protein nb.	adj. p-value	FC
(7) 227620	1.4e-4	2.03
(2) 203600	1.4e-4	1.89
(3) 275440	1.4e-4	1.97
(9) 227280	2.3e-4	1.82
(16) 270250	2.4e-4	2.08
(17) 315320	3.3e-4	1.64
(18) 297880	4.3e-4	2.06
(14) 212300	4.8e-4	1.64
(1) 224460	4.8e-4	2.28
(19) 208830	4.8e-4	1.64
(20) 291600	9.4e-4	1.57
(21) 222170	0.002	1.87
(15) 203310	0.003	1.58
(10) 270240	0.003	1.77
(22) 304955	0.004	1.47

AAQc

protein nb.	adj. p-value	FC
(23) 286450	4.3e-5	2.70
(24) 310780	1.1e-4	2.65
(3) 275440	1.1e-4	1.98
(10) 270240	1.1e-4	1.93
(9) 227280	1.5e-4	2.13
(18) 297880	1.7e-4	2.27
(1) 224460	2.2e-4	2.84
(25) 220240	2.2e-4	2.12
(26) 210280	5.1e-4	2.37
(8) 251540	5.1e-4	1.85
(12) 220950	7.0e-4	1.61
(16) 270250	7.4e-4	1.75
(7) 227620	0.001	1.65
(27) 217680	0.001	1.69
(28) 239740	0.001	1.48

protein nb.	name	hyper LOPIT
(1) 224460	AminoPep	NA
(2) 203600	GRA50	DG
(3) 275440	GRA6	DG
(4) 237880	GRA13	DG
(5) 244280	hypoth.	NA
(6) 277270	NTPase II	DG
(7) 227620	GRA2	DG
(8) 251540	GRA9	DG
(9) 227280	GRA3	DG
(10) 270240	MAG1	DG
(11) 319340	GRA52	DG
(12) 220950	MAF1	DG
(13) 215980	hypoth.	NA
(14) 212300	GRA32	DG
(15) 203310	GRA7	DG
(16) 270250	GRA1	DG
(17) 315320	SRS52A	PM
(18) 297880	GRA23	DG
(19) 208830	GRA16	DG
(20) 291600	GILT	EV
(21) 222170	GRA17	DG
(22) 304955	PPM11C	DG
(23) 286450	GRA5	DG
(24) 310780	GRA4	DG
(25) 220240	GRA31	DG
(26) 210280	Ark1	NA
(27) 217680	GRA57	DG
(28) 239740	GRA14	DG

Figure 7: Knockdown of apical annuli membrane proteins results in accumulation of dense granule proteins in the parasite. (A) Volcano plots showing the changes of abundance of cell proteins with three apical annuli proteins depleted over 24 hours of auxin treatment compared to untreated controls (N=3). Black dots represent measures for individual cell proteins other than dense granule proteins, red and orange dots indicate dense granule proteins assigned by hyperLOPIT (red = statistically significant changes, orange = non-significant changes, using adjusted p-values) (Barylyuk et al., 2020). (B) The 15 most significantly increased proteins with each apical annuli protein knockdown amount to 28 common proteins randomly sampled by the shotgun proteomics, all but 6 of which are known dense granule proteins. Red bracketed numbers indicate GRAs, black bracketed numbers non-GRAs. FC, fold change; protein nb., VEuPathdb gene identifiers; hypothe., hypothetical protein; DG, dense granule; EV, endomembrane vesicles; PM, plasma membrane; NA, not assigned a location by hyperLOPIT. See Table S2 for full quantitative proteomics data.

Discussion

The *Toxoplasma* apical annuli have been previously described as features of the cell's inner membrane complex, beneath and separate from the plasma membrane. Here we show that the annuli structures are relevant to the plasma membrane with four integral plasma membrane proteins at these sites including one that is exposed at the cell surface. We show that the annuli occur at small gaps in the IMC where three alveolar vesicles meet (the apical cap vesicle and two lateral vesicles) providing direct access of the cytosol to the plasma membrane. One of the apical annuli membrane proteins, *Tg*LMBD3, is a polytopic protein conserved throughout Apicomplexa and most eukaryotes. The other three represent Q SNARE proteins, containing Qa, Qb, and Qc SNARE motifs respectively, which are tethered by C-terminal transmembrane domains as is their conventional and ancestral state (SNARE protein fusions, and alternative membrane tethering mechanisms via post-translational added moieties, occur in many systems as derived states) (Jahn and Scheller, 2006; Neveu et al., 2020). Depletion of all four of these

370 proteins inhibits dense granule secretion firmly implicating the apical annuli as the site of dense
371 granule docking and membrane fusion.
372
373 The LMBD protein presents the first identified apical annuli protein that could interact with
374 extracellular ligands and molecules. The functions of this group of proteins, however, are not well
375 understood (Redl and Habeler, 2022). The four clear LMBD protein orthogroups found
376 throughout eukaryotes suggest that the last eukaryotic common ancestor (LECA) contained
377 multiple of these proteins. While some eukaryotes, e.g. *Dictyostelium*, have retained genes for all
378 four (Kelsey et al., 2012), most major eukaryotic groups have lost one or more of these
379 paralogues. The first identified protein of this family, LMBR1, was associated with polydactyly
380 and limb malformations in vertebrates, but its molecular role is still unclear (Gyimesi and
381 Hediger, 2022). Other known members of the family are: LMBR1-like (LMBR1L, also known as
382 LIMR), which interacts with lipocalins and other ligands involved in signalling cascades (Wnt/b-
383 catenin and Nf-kB pathways); LMBR1 domain containing protein 1 (LMBD1), which interacts with
384 the lysosomal cobalamin transporter ABCD4; and LMBD2, which is a G-protein coupled
385 receptor-associated regulator of β2-adrenoceptor signalling (Gyimesi and Hediger, 2022). While
386 *Tg*LMBD3 is in a different orthogroup to any of these studied paralogues, their common
387 involvement in signalling events suggests that this protein of the apical annuli could contribute to
388 the regulation of dense granule secretion, potentially in response to some extracellular stimulus.
389
390 SNARE proteins are classically responsible for driving membrane fusion events and our data
391 strongly implicate the roles of *Tg*AAQa, *Tg*AAQb, and *Tg*AAQc with dense granule fusion with
392 the plasma membrane at the apical annuli. Molecular phylogenies place these three SNAREs
393 with canonical orthologues: *Tg*AAQa with Syntaxin2 orthologues, *Tg*AAQb with NPSN11/Syp7
394 orthologues, and *Tg*AAQc with SYP71 ortholgoues, and there is no evidence of duplication
395 and/or specialisation of these SNAREs in Apicomplexa (Klinger et al., 2022). Vesicle fusion to a
396 target membrane is driven through the regulated formation of the SNARE-complex, a tight four-
397 helix bundle of the Qa, Qb and Qc SNARE motifs with an R SNARE motif-containing protein
398 (Jahn and Scheller, 2006; Neveu et al., 2020). The Q SNAREs are anchored to the target
399 membrane, and this is consistent with our observation of all three *Tg*AAQ SNAREs being stably
400 associated at the apical annuli. Moreover, our hyperLOPIT spatial proteomic data assigned all
401 three as integral proteins of the plasma membrane, so it is unlikely that these SNAREs mediate
402 any direct interaction with the IMC alveolar vesicle membranes despite their proximity (Barylyuk
403 et al., 2020). It is curious that the knockdown phenotypes of the three SNAREs differ, with
404 *Tg*AAQa showing a much faster arrest of parasite replication. We note that this SNARE, and
405 *Tg*AAQc, show evidence of a second location in the cell. Some SNARE proteins are known to be
406 able to participate in multiple membrane fusion events at different parts of the cell and with
407 different SNARE partners (Jahn and Scheller, 2006), so a second (or more) role for the *Tg*AAQ
408 SNAREs might explain their different growth phenotypes upon knockdown. In none of our
409 SNARE knockdowns did we see changes to the biogenesis of rhoptries or micronemes, two
410 other post-Golgi compartments, so these SNAREs do not perform essential roles in these
411 processes. The growth retardation with apical annuli protein depletion, particularly *Tg*LMBD3 and
412 *Tg*AAQb which are exclusive to the these sites, is consistent with the failure of delivery of dense
413 granule proteins that are required in the parasitophorous vacuole membrane for harvesting host
414 materials for the parasites' nutrition (Griffith et al., 2022).
415
416 Vesicle fusion typically requires an R SNARE that is anchored in the vesicle membrane, but we
417 currently have not identified a candidate for the dense granules. However, other molecules
418 contribute to the trafficking and delivery of vesicles to their sites of fusion (Koike and Jahn,
419 2022), and Rab11A has been identified to play this role for dense granules. Rab11A was shown

420 to collocate with dense granules and track their active movement along cytoskeletal fibres.
421 Furthermore, loss of function of Rab11A blocks dense granule protein secretion (Venugopal et
422 al., 2020). Accompanying this block, an increase in dense granule numbers in the parasite's
423 cytoplasm was seen, similar to what we saw with *Tg*AAQ SNARE knockdown by both
424 microscopy and quantitative proteomics. Furthermore, a concurrent study of *Toxoplasma*
425 SNAREs has shown that knockdown of the *Tg*AAQ SNAREs results in Rab11A accumulating at
426 the apical annuli (Fu et al., 2023), consistent with Rab11A being required for dense granule
427 delivery and the SNAREs mediating subsequent vesicle fusion.
428
429 The evidence of a second bespoke structure for vesicle exocytosis within the elaborate
430 apicomplexan pellicle of *Toxoplasma* tachyzoites raises the question, why is the apical complex
431 not sufficient? Both micronemes and rhoptries are known to pass through the conoid and
432 exocytose at the apical plasma membrane via dedicated docking and fusion machinery (Aquilini
433 et al., 2021; Dubois and Soldati-Favre, 2019; Giuliano et al., 2023; Suarez et al., 2019). Could
434 dense granules not use this same site? The outcomes of each type of organelle secretion might
435 be the reason why not. Microneme secretion from parasites within their host cells triggers
436 parasite egress through permeabilization of the host membranes prior to motile escape (Roiko et
437 al., 2014). Dense granule secretion, on the other hand, is required to actively maintain a stable
438 intracellular host environment in which the parasite is nourished for replication (Griffith et al.,
439 2022). The incompatibility of these two processes might, therefore, have driven their physical
440 separation. Moreover, these pre- and post-invasion secretion processes are also biochemically
441 separated because both microneme and rhoptry secretion are SNARE-independent. It is known
442 that individual SNARE proteins can often form complexes with multiple different SNARE-complex
443 types, and this promiscuity could potentially allow some 'leaky' secretion between organelle
444 types were they all SNARE-mediated. Even for micronemes and rhoptries the processes of
445 docking and exocytosis are radically different despite operating at the same site (Cova et al.,
446 2022; Dubois and Soldati-Favre, 2019). Thus, the consequences of mistiming of any of these
447 events might be the basis for the multiple levels of separation, including dense granules from the
448 separate sites of the apical annuli.
449
450 With the discovery of the site of dense granule secretion, the regulation of this critical process
451 can now come under closer scrutiny. Dense granule protein secretion has previously been
452 described as constitutive or unregulated, however, it was subsequently observed to be
453 negatively regulated by Ca^{2+} in a reciprocal manner to the positive Ca^{2+}-driven exocytosis of
454 micronemes (Katris et al., 2019). Centrin2 forms a ring at the inner side of the apical annuli, and
455 Ca^{2+}-mediated constriction of centrin fibres might contribute to the closure of the annuli and
456 inaccessibility of the plasma membrane to vesicles or docking machinery. Several other ring-
457 forming components of the inner apical annuli structures contain cyclic nucleotide binding
458 domains, multiple phosphorylation sites, and other putative domains (rabaptin, gametogenetin)
459 that could participate in vesicle trafficking and docking (Engelberg et al., 2020). Both Ca^{2+} and
460 cyclic nucleotides function as important messenger molecules that drive complex phospho-
461 signalling cascades in apicomplexans that are at the heart of their invasion and proliferation
462 programmes (Bisio and Soldati-Favre, 2019; Uboldi et al., 2018). These features of apical annuli
463 proteins are, therefore, consistent with apical annuli being wired into these regulatory networks. It
464 is possible that *Tg*LMBD3 might play a further role in regulation potentially responding to external
465 cues. Dense granules are believed to contain upwards of 120 different cargo proteins in *T. gondii*
466 (Barylyuk et al., 2020) so the coordination of release of this complex cargo into the host seems
467 likely to be under strong selective constraints.
468

Where, then, did the apical annuli come from, and in what other related organisms might they occur? *Toxoplasma* and its very close relatives (*Hammondia, Neospora*) are relatively unusual in maintaining their complex cell pellicle throughout their asexual replication cycle (Gubbels et al., 2021; Sheffield and Melton, 1968; Striepen et al., 2007). While many other apicomplexans differentiate to lose the IMC as they feed and grow within their host's cells, *Toxoplasma* remains fully invasion-ready at all stages of growth. This maintenance of IMC, micronemes, rhoptries and the apical complex, concurrent with the secretion of dense granule proteins, might necessitate the presence of apical annuli as alternative secretion points. *Eimeria* spp. on the other hand, do lose their IMC after sporozoites invade the host's gut epithelial cells, and yet, freeze fracture studies of *Eimeria* sporozoite surfaces show apical annuli that look very similar to the structures in *Toxoplasma* (Dubremetz and Torpier, 1978) and apical annuli proteins AAP1-5 are all present in *Eimeria* (Engelberg et al., 2020). The presence of these structures in *Eimeria* might be because when sporozoites invade their hosts there is a delay of multiple hours before the IMC is lost (Pacheco et al., 1975). The need for rapid post-invasion secretion of proteins that establish a safe and productive host environment, including defence against host immune attack, might therefore require apical annuli as secretion points even before the IMC and apical complex are dismantled. In turn, many other apicomplexans might require such secretion points to account for the fast pace of events from invasion to host modification that might need to precede IMC disassembly. Moreover, the delivery of plasma membrane carrier proteins and surface GPI-tethered molecules have implicated Rab11A, the *Tg*AAQ SNAREs and, therefore, the apical annuli in these further secretory pathways (Fu et al., 2023; Venugopal et al., 2020). Other apicomplexans might similarly have need for such secretion even in their invasion-ready cell forms. While some of the *Toxoplasma* apical annuli proteins appear more restricted to the Coccidia, this might primarily reflect the fast evolution of these structural proteins, many of which include coiled-coil domains (Engelberg et al., 2020). *Tg*LMBD3, on the other hand, is universally present in apicomplexans and their close relatives including the dinoflagellates that also have clear apical complexes with microneme and rhoptry-type secretory organelles by ultrastructural studies (Pacheco et al., 2020). It is possible that a much wider presence of apical annuli has been overlooked owing to their structure being more inconspicuous to traditional microscopy methods.

Acknowledgments

This work was supported by the Wellcome Trust, United Kingdom, Investigator award 214298/Z/18/Z to RFW. We thank VEuPathDB for their invaluable Informatics Resources, and Jan Pyrih and Brandon Mercado-Saavedra for useful discussions.

Methods

Growth and generation of transgenic *T. gondii*

T. gondii tachyzoites from the strain RH and derived strains, including RH Δku80/TATi (Sheiner et al., 2011), were maintained at 37ºC with pCO_2 of 10% growing in human foreskin fibroblasts (HFFs) cultured in Dulbecco's Modified Eagle Medium supplemented with 1% heat-inactivated fetal bovine serum, 10 unit ml^{-1} penicillin, and 10 µg ml^{-1} streptomycin, as described elsewhere (Roos et al., 1994). When appropriate for selection, chloramphenicol was used at 20 µM, and pyrimethamine at 1 µM. Reporter protein-tagging of gene loci with reporters 6xHA, 3xv5 and eGFP was done according to our previous work (Barylyuk et al., 2020). For protein function tests

518 by gene knockdowns, the mini auxin-inducible degron (mAID) cassette was fused to either the C-
519 or N-terminus in Tir1 transgenic line using the same strategy as for reporter protein-tagging
520 (Koreny et al., 2023). Proteins of interest were depleted with the addition of the auxin, 3-
521 indolacetic acid (IAA), at a final concentration of 500 µM. Oligonucleotides used for all gene
522 modifications are shown in Table S3.
523
524 **Immunofluorescence microscopy**

525 *T. gondii*-infected HFF monolayers grown on glass coverslips were fixed with 2% formaldehyde
526 at room temperature for 15 min and permeabilized with 0.1% TritonX-100 for 10 min, except for
527 GRA5 detection where 0.002% digitonin was used instead to selectively detect secreted GRA5.
528 Blocking was done with 20% FBS for 1 hr, and the coverslips were then incubated with a primary
529 antibody for 1 hr, washed in blocking buffer, followed by 1 hr incubation with a secondary
530 antibody. Coverslips were mounted using ProLong Diamond Antifade Mountant (ThermoFisher
531 Scientific, Massachusetts, USA). Images were acquired using a Nikon Eclipse Ti widefield
532 microscope with a Nikon objective lens (Plan APO, 100×/1.45 oil) and a Hamamatsu C11440,
533 ORCA Flash 4.0 camera. 3D structured illumination microscopy (3D-SIM) was implemented on a
534 DeltaVision OMX V4 Blaze (GE Healthcare, Issaquah, California, USA) with samples prepared
535 as for widefield immunofluorescence assay (IFA) microscopy with the exception that High
536 Precision coverslips (Marienfeld Superior, No1.5H with a thickness of 170 µm ± 5 µm) were used
537 in cell culture, and Vectashield (Vector Laboratories, Burlingame, California, USA) was used as
538 mounting reagent. Samples were excited using 405, 488, and 594 nm lasers and imaged with a
539 100x oil immersion lens (1.42 NA). The 3D-SIM images were reconstructed in softWoRx
540 software version 6.1.3 (Applied Precision). All fluorescence images were processed using Image
541 J software (http://rsbweb.nih.gov./ij/). The antibodies used, source and the relevant
542 concentrations are described in Table 4.
543
544 **Phylogenetic analyses**

545 For the phylogenetic analyses, sequences were aligned using Mafft v7.407 with the L-INS-i
546 algorithm (Katoh and Standley, 2013). Alignments were edited manually using Jalview
547 (https://www.jalview.org). Maximum-likelihood (ML) trees were calculated using PhyML-3.1 with
548 bootstrap (1000 iterations) or SH-like aLRT branch supports (Guindon et al., 2010).
549
550 **Plaque assay**

551 To test lytic cycle competence of knockdown cell lines by plaque formation in HFF monolayers,
552 200 freshly lysed parasites were added to 6-well plates containing HFF monolayers. IAA was
553 added to induce the gene knockdown, or an equivalent volume of ethanol added for uninduced
554 controls. After 7 days of growth, flasks were aspirated, washed once with PBS, fixed with 5 ml of
555 100% methanol for 5 mins and stained with 5 ml of 1% crystal violet solution for 15 mins. After
556 staining, the crystal violet solution was removed, and the flasks were washed three times with
557 PBS, dried and imaged.
558
559 **Replication assay**

560 The parasites were pre-treated with IAA (*Tg*LMBD3: 12 hrs, *Tg*AAQb: 6 hrs, *Tg*AAQa: 3 hrs,
561 *Tg*AAQc: 6 hrs) or an equivalent volume of ethanol for the uninduced control before egress from
562 the host cell to deplete the proteins of interest. Intracellular tachyzoites were then harvested
563 through needle-passage using a 27G hypodermic syringe needle and seeded on the HFF
564 monolayer growing on coverslips in 6-well plates. After 2 hrs, uninvaded parasites were removed
565 by washing and the invaded parasites were allowed to grow for further 24 hrs with auxin or

566 ethanol, followed by fixation for 20 mins with 2% paraformaldehyde. Coverslips were then
567 imaged using a Nikon Eclipse Ti microscope with a Nikon objective lens (Plan APO, 100
568 x/1.45 oil), and a Hamamatsu C11440, ORCA Flash 4.0 camera. In haphazardly selected fields,
569 the number of parasites per parasitophorous vacuole was scored. A minimum of 200
570 parasitophorous vacuoles was scored for each of the three biological replicates. P-values were
571 calculated with multiple t-tests and corrected for multiple comparisons using the Holm-Sidak
572 method in GraphPad Prism, v9 (GraphPad, California USA). A p-value of <0.05 was considered
573 as significant.
574
575 **Trypsin shaving assay**

576 The trypsin shaving assay was adapted from (Jia et al., 2017) Fresh tachyzoite pellets were re-
577 suspended in 0.1% trypsin/EDTA and incubated at 37ºC for 1 hr, 2 hrs and 4 hrs, and the control
578 was treated with PBS only. After the incubation, samples were spun at 3000x*g* for 8 mins, and
579 supernatants were removed. Pellets were resuspended in 1 x Nupage LDS Sample buffer with
580 either 50 mM DTT (followed by heated at 75 ^{0}C for 10 mins) or with 10 mM Tris(2-carboxyethyl)
581 phosphine hydrochloride (Sigma) (followed by incubation at room temperature for 2 hours).
582 Western blots were performed using rat anti-HA, mouse anti-Sag1, rabbit anti-GAP40, rabbit
583 anti-PRF and rabbit anti-Tom40 antibodies.
584
585 **Proteomics**

586 *BioID Sample preparation*
587 For the proximity biotinylation assay, we generated a *T. gondii* cell line (in parental line RH
588 Δku80) by endogenous tagging of the *Tg*LMBD3 locus with the in-frame coding sequence for the
589 promiscuous bacterial biotin ligase, BirA*. The parental cell line was used as a negative control
590 in biotin treatments. We followed the previously published BioID protocols (Chen et al., 2015;
591 Koreny et al., 2021). Briefly, the parasites were grown in three biological replicates in elevated
592 biotin concentration (150 µM) for 24 hrs prior to egress, separated from the host-cell debris and
593 washed 5x in phosphate-buffered saline. The cell pellets were lysed in RIPA buffer by sonication
594 and the lysates containing ~5 mg of total protein were incubated with 250 µl of unsettled
595 Pierce™ Streptavidin Magnetic Beads (Thermo-Fisher: 88817) overnight at 4°C with gentle
596 agitation. The beads were then sequentially treated as follows: washed 3x in RIPA, 1x in 2 M
597 UREA and 100 mM triethylammonium bicarbonate (TEAB; Sigma); washed 3x in RIPA; reduced
598 in 10 mM DTT and 100 mM TEAB for 30 min at 56°C; alkylated in 55 mM iodoacetamide 100
599 mM TEAB for 45 min at room temperature in the dark; and washed in 10 mM DTT 100 mM
600 TEAB, followed by 2x 15 min in 100 mM TEAB with gentle agitation. The peptides were digested
601 on the beads by a 1 hr 37°C incubation in 1 µg of trypsin dissolved in 100 mM TEAB, followed by
602 an overnight 37°C incubation after adding an extra 1 µg of trypsin.
603
604 *Whole-cell quantitative proteomics Sample preparation*
605 Intracellular tachyzoites were pre-treated with or without IAA prior to egress to deplete annuli
606 proteins individually as for the replication assays (*Tg*LMBD3: 12 h, *Tg*AAQb: 6 h, *Tg*AAQc: 6 h).
607 These were then harvested through needle-passage as before, seeded onto T175 flasks and
608 allowed to proliferate for further 24 hrs with or without continued IAA treatment. Approximately 40
609 million parasites were then harvested by needle-passage into Endo buffer (44.7 mM K_2SO_4, 10
610 mM $MgSO_4$, 106 mM sucrose, 5 mM glucose, 20 mM Tris-H_2SO_4, 3.5 mg/ml BSA, pH 8.2) to
611 mimic intracellular conditions. Host cell debris was removed by filtration through a 3 µm filter and
612 tachyzoites were harvested by centrifugation at 1500x*g* for 10 minutes . Pellets were lysed in 8M
613 urea prepared in 20 mM HEPES buffer and sonicated for 5 cycles (50s ON, 50s OFF). Samples
614 were reduced by the addition of DTT to a final concentration of 5 mM and incubated at 30 mins

615 at 37°C. A final concentration of 15 mM iodoacetamide was added to alkylate the samples and
616 incubated in the dark for 30 minutes. Proteins were then digested by the addition of trypsin/LysC
617 mix at of 25 :1 protein:protease ratio (w/w) and incubation for 4 hrs at 37°C. The reaction was
618 then diluted at 8-fold or greater by adding 20 mM HEPES, pH 8 to reduce the concentration of
619 urea to 1M, and incubation at 37°C was continued overnight. Peptide digestion was terminated
620 with a final concentration of 1% trifluoracetic acid (TFA). Particulate material was pelleted by
621 centrifugation at 21000x*g*, 4°C, 10 mins, and the supernatant was recovered for peptide
622 desalting using Pierce™ Peptide Desalting Spin Column (ThermoFisher: 89851) as described by
623 the manufacturer. Peptide concentration was measured using the Pierce™ Quantitative
624 Fluorometric Peptide Assay (ThermoFisher: 23290) according to the manufacturer's instructions.
625 From each sample, a volume containing 17 µg amount of peptide was dried in a vacuum
626 centrifuge (SpeedVac SPD 1030), then re-suspended in 100 µl of 100 mM TEAB solution, pH
627 8.5.
628
629 *TMT-labelling and liquid chromatography and tandem mass spectrometry*
630 TMT-labelling was done using either a TMT10plex isobaric tagging reagent (ThermoFisher:
631 90110) for BioID samples, or TMTpro™ 16 plex Label Reagent Set 1 x 5 mg (ThermoFisher:
632 A44520) for whole-cell protein quantitation. Each TMT reagent vial containing 0.5 mg of the
633 labelling reagents was brought to room temperature and dissolved in 40 µl of LCMS-grade
634 acetonitrile immediately before use. The TMT reagents were then split to two sets and 20 µl of
635 the TMT reagents were added to each peptide sample. After incubating for 1 hr at room
636 temperature, 5 µl of 5% hydroxylamine (v/v) was added to each sample, followed by incubation
637 for 15 mins to quench the reaction. The TMT-labelled fractions were combined and dried in a
638 vacuum centrifuge (SpeedVac SPD 1030) at 4°C.
639
640 LCMS analyses were carried out on an Orbitrap™ Fusion™ Lumos™ Tribrid™ mass
641 spectrometer coupled on-line with a Dionex Ultimate™ 3000 RSLCnano system (Thermo Fisher
642 Scientific) as previously described (Barylyuk et al., 2020). The XCalibur v3.0.63 software was
643 used to control the instrument parameters and operation, and record and manage the raw data.
644 The LCMS system was operated in the positive-ion data-dependent acquisition mode with the
645 SPS-MS^3 acquisition method with a total run time of 120 min. The dried TMT10 plex-labelled
646 peptide samples resolubilised in an LC-MS sample loading solution (0.1% aqueous formic acid)
647 at a concentration of approximately 1 µg/µl. Approximately 1 µg of the sample was loaded onto a
648 micro-precolumn (C18 PepMap 100, 300 µm i.d. × 5 mm, 5 µm particle size, 100 Å pore size,
649 Thermo Fisher Scientific) with the sample loading solution for 3 min. Following the loading step,
650 the valve was switched to the inject position, and the peptides were fractionated on an analytical
651 Proxeon EASY-Spray column (PepMap, RSLC C18, 50 cm × 75 µm i.d., 2 µm particle size, 100
652 Å pore size, Thermo Fisher Scientific) using a linear gradient of 2-40 % (vol.) acetonitrile in
653 aqueous 0.1% formic acid applied at a flow rate of 300 nl/min for 95 min, followed by a wash step
654 (70% acetonitrile in 0.1% aqueous formic acid for 5 min) and a re-equilibration step. Peptide ions
655 were analyseed in the Orbitrap at a resolution of 120,000 in an m/z range of 380-1,500 with a
656 maximum ion injection time of 50 ms and an AGC target of 4E5 (MS^1 scan). Precursor ions with
657 the charge states of 2-7 and the intensity above 5,000 were isolated in the quadrupole set to 0.7
658 m/z transmission window and fragmented in the linear ion trap via collision-induced dissociation
659 (CID) at a 35% normalised collision energy, a maximum ion accumulation time of 50 ms and an
660 AGC target of 1E4 (MS^2 scan). The selected and fragmented precursors were dynamically
661 excluded for 70 secs. Synchronous precursor selection (SPS) was applied to co-isolate ten MS^2-
662 fragments in the linear ion trap with an isolation window of 0.7 m/z in the range of m/z 400-1,200,
663 excluding the parent ion and the TMT reporter ion series. The SPS precursors were activated at
664 a normalized collision energy of 65% to induce fragmentation via high-collision energy

665 dissociation (HCD). The product ions were measured in the Orbitrap at a resolution of 50,000 in
666 a detection range of m/z 100-500 with a maximum ion injection time of 86 ms and an AGC of
667 5E4 (MS^3 scan). The mass spectrometry proteomics data have been deposited to the
668 ProteomeXchange Consortium via the PRIDE (Perez-Riverol et al., 2021) partner repository with
669 the dataset identifier PXD034193.
670
671 *Raw LCMS data processing*
672 The processing of BioID raw LCMS data for peptide and protein identification and quantification
673 was performed with Proteome Discoverer v2.3 (Thermo Fisher Scientific). Raw mass spectra
674 were filtered, converted to peak lists by Proteome Discoverer and submitted to a database
675 search using Mascot v2.6.2 search engine (Matrix Science) against the protein sequences
676 of *Homo sapiens* (93,609 entries retrieved from UniProt on 09.04.2018), *Bos taurus* (24,148
677 entries retrieved from UniProt on 17.04.2017), and *Toxoplasma gondii* strain ME49 (8,322
678 entries retrieved from ToxoDB.org release 36 on 19.02.2018) (Amos et al., 2021). Common
679 contaminant proteins – e.g., human keratins, bovine serum albumin, porcine trypsin – from the
680 common Repository of Adventitious Proteins (cRAP, 123 entries, adapted
681 from https://www.thegpm.org/crap/) were added to the database, as well as the sequence of the
682 BirA* used to generate the BioID bait proteins by gene fusion. The precursor and fragment mass
683 tolerances were set to 10 ppm and 0.8 Da, respectively. The enzyme was set to trypsin with up
684 to two missed cleavages allowed. Carbamidomethylation of cysteine was set as a static
685 modification. The dynamic modifications were set to TMT6plex at the peptide N-terminus and
686 side chains of lysine, serine, and threonine, oxidation of methionine, deamidation of asparagine
687 and glutamine, and biotinylation of the peptide N-terminus or lysine side chain. The false
688 discovery rate of peptide-to-spectrum matches (PSMs) was validated by Percolator v3.02.1 (The
689 et al., 2016) and only high-confidence peptides (FDR threshold 1%) of a minimum length of 6
690 amino acid residues were used for protein identification. Strict parsimony was applied for protein
691 grouping. TMT reporter ion abundances were obtained in Proteome Discoverer using the most
692 confident centroid method for peak integration with 20 p.p.m. tolerance window. The isotopic
693 impurity correction as per the manufacturer's specification was applied. For protein
694 quantification, PSMs with precursor co-isolation interference above 50% were discarded, and the
695 TMT reporter ion abundances determined for unique (sequence found in proteins belonging to a
696 single protein group) and razor (if sequence is shared by protein belonging to multiple protein
697 groups, the quantification result is attributed to the best-associated Master Protein) peptides
698 were summed.
699
700 The processing of whole-cell protein quantitation raw LCMS data for peptide and protein
701 identification and quantification was performed with Proteome Discoverer v2.5 (Thermo Fisher
702 Scientific). SequestHT was used as a search engine with set mass tolerances for peptide
703 precursor and fragment ions of 10 ppm, and 0.5 Da, respectively. Tryptic peptides were allowed
704 to have 2 missed cleavage sites. Mass shifts were set up as either static modification for cysteine
705 carbamidomethylation (+57.021 Da) and lysine TMTpro label (+304.207 Da) or as dynamic
706 modification for methionine oxidation (+15.995 Da), asparagine and glutamine deamidation
707 (+0.984 Da), and peptide N-terminal TMTpro label (304.207 Da). Percolator was used for false
708 discovery rate (FDR) estimations with a fixed target FDR of 1%. All peptide-spectrum matches
709 (PSM) up to delta Cn value of 0.05 were initially considered and only high-confidence peptides
710 were retained. Contaminant proteins were removed. Quantification of peptides at the MS3 level
711 was performed using Most Confident Centroid as integration method (tolerance of 20 ppm).
712 Reporter Abundance was based on signal-to-noise (S/N) values and corrected for isotopic
713 impurities of TMT reagents according to manufacture specifications (TMTpro 16plex LOT
714 #VJ313476). Protein grouping was carried out applying the strict parsimony principle and

proteins with high (q ≤ 0.01) and medium (q ≤ 0.05) confidence retained. The PD PSM output file was filtered and aggregated manually using R Bioconductor packages. PSMs were filtered for uniqueness (Number.of.Protein.Groups = 1), rank (Concatenated.Rank = 1), ambiguity (Unambiguous+Selected), isolation interference (≤75%), average S/N (≥10), and SPS mass match percentage (≥70%) and aggregated to protein level applying robustSummary. Global protein abundances between samples were median aligned to account for slight variabilities due to peptide loading per TMT channel.

Raw LC-MS data and PD search results have been deposited to the ProteomeXchange Consortium (http://proteomecentral.proteomexchange.org) via the PRIDE partner repository (Perez-Riverol et al. 2022) with the dataset identifiers PXD034193 and PXDxxxxxx.

Statistical analysis of proteomic data

BioID data analysis was performed with *R* v3.6.1 using packages *tidyverse*v1.2.1 for data import, management, and manipulation, *Bioconductor* packages *MSnbase* v2.10.1 for managing quantitative proteomics data, *biobroom* v1.16.0 (https://github.com/StoreyLab/biobroom) for converting *Bioconductor* objects into *tidy data frames*, and *limma* v3.40.6 (Ritchie et al., 2015) for linear modelling and statistical data evaluation, as previously described (Koreny et al., 2023). The protein-level report generated by Proteome Discoverer was imported into R and filtered to remove non-*Toxoplasma* and low-confidence (protein FDR confidence level “Low”, q ≥ 0.05). Only Master Proteins with a complete set of TMT abundance values across three replicates of the BioID bait and control samples were considered for the analysis. The protein abundance values in each biological sample were corrected for the total amount using normalisation factors derived from the abundances of two proteins, acetyl-CoA carboxylase ACC1 (TGME49_221320) and pyruvate carboxylase PC (TGME49_284190). Both proteins are highly expressed, endogenously biotinylated, and reside in the matrix of subcellular compartments, the apicoplast and mitochondrion for ACC1 and PC, respectively, where they are not accessible to the BirA*-fused BioID baits. Hence, these two proteins served as suitable internal standards. The normalised protein abundances were log2-transformed and modelled as a simple linear relationship between the abundances described by a constant factor (intercept), which is of no interest to us, and the condition (BirA*-tagged vs. control) using *limma*. If the condition parameter estimated by *limma* linear model was significantly different from zero, we concluded that the condition (presence of the BirA*-fused bait) had a significant effect on the protein abundance. Also, *limma* estimated the model parameters taking into account the relationship between protein average intensities and the variance (low-abundance proteins tend to have a greater variance) by empirical Bayesian shrinking of the standard errors towards the trend. This enabled a better control of false discoveries and outliers affording more robust identification of significantly enriched proteins. The resulting *p*-values were adjusted for multiple testing using the Benjamini-Hochberg method (FDR < 1 %).

For whole-cell protein quantitation, differential protein abundance between control and treated cell lines for *Tg*LMBD3-mAID-3xV5, mAID-3xV5-*Tg*AAQb and mAID-3xV5-*Tg*AAQc was determined by implementing the Bioconductor package *limma*, using a mean reference model with the lmFit and eBayes functions. Proteins with an adjusted p-value < 0.05 (Benjamini-Hochberg correction) after moderated t-tests were considered significant. The complete R markdown file used for the analysis is provided (Data file S1).

Supplemental material

Table S1: BioID Supplementary data file. Sheet 1: BioID_significant_changes: Columns show ToxoDB accession number, log2-fold change (logFC) with left and right confidence intervals (CI.L, CI.R), the average log2-abundance value of this protein across treatments and their replicates (AveExpr), the moderated t-statistics value (t), the raw p-value (P.Value), the adjusted p-value (adj.P.Val), and the log-odds that the protein is differentially abundant (B). Sheet 2: Normalised TMT intensity values for three LMBD3-BirA* biological replicates (RUN1-3) each with three parental control samples.

Table S2: Quantitative proteomics Supplementary data file. Sheets 1-3 give data for the three cell lines: TgLMBD-mAID-3xV5, mAID-3xV5-TgAAQb and mAID-3xV5-TgAAQc. Columns show ToxoDB accession number, log2-fold change between treatment and control (logFC), the average log2-abundance value of this protein across treatments and their replicates (AveExpr), the moderated t-statistics value (t), the raw p-value (P.Value), the adjusted p-value (adj.P.Val), the log-odds that the protein is differentially abundant (B), the protein description (Description), and the tagm-predicted subcellular location according to the ToxoLOPIT map of (Barylyuk et al., 2020).

Table S3: Primers and plasmids for genetic modifications.

Table S4: Antibodies used for IFAs and Western blots.

Figure S1: Maximum likelihood phylogenies of the LMBR1 domain-containing proteins from Figure 1. (A) All LMBR1 domain-containing proteins can be divided into four different orthogroups. Numbers at branches are bootstrap/aLRT SH-like supports for the monophylies of the four orthogroups. Sequences of the *Plasmodium* spp. from the orthogroup I are at the base of the orthogroup and outside of the cohort of sequences that represent the other Apicomplexa, including TgLMBD3. This is likely caused by a long-branch attraction (LBA) artefact, which pulls the fast-evolving *Plasmodium* sequences towards the sequences from the other orthogroups. Nevertheless, the placement of these *Plasmodium* sequences within the orthogroup I is well supported. The LBA artefact is diminished by computing the phylogenetic tree from an alignment of the sequences solely from the orthogroup I (B). Here, *Plasmodium* spp. is within the monophyletic Apicomplexa. Furthermore, monophyly of Alveolata (Ciliates + Myzozoa[Apicomplexa, Chrompodelids, Perkinsids, Syndiniales, Dinoflagellates]) and monophyly of SAR (Stramenopiles, Alveolata, Rhizaria) clade are also supported, suggesting vertical evolution of the LMBD3 gene from LECA (last eukaryotic common ancestor) into current eukaryotic lineages. aLRT SH-like supports are shown only for the relevant branches that constitute higher order taxa annotated in the figure.

Figure S2: Abundance and distribution of rhoptry and microneme proteins are unaffected when apical annuli membrane proteins are knocked down. Wide-field immuno-fluorescence assays of MIC2 and ROP1 without (control) or with auxin-induced protein knockdown for the four apical annuli membrane proteins. Assays for MIC2 and ROP1 were done 24 hours after invasion. Scale bar = 5 µm.

Figure S3: Western blot and PCR analysis validating correct epitope-tag integration. (A) Western blots of cell lysates using anti-v5 antibody shows *Tg*AAQb, *Tg*AAQa, and *Tg*AAQc were successfully tagged with 3xv5. (B) PCR showing successful integration of epitope tag in the intended locus for each apical annuli SNARE protein. For *Tg*AAQb, *Tg*AAQa, *Tg*AAQc, a

universal forward primer that anneals in the promoter region is used together with a gene-specific reverse primer to obtain a PCR product. For *Tg*LMBD3, a gene-specific forward primer is used together with a reverse primer annealing in the terminator region. Products obtained are the expected size for each reaction. Parental cell lines for the transfection are used as a negative control.

Data file S1: R markdown file of analytical workflow of quantitative proteomics data. The markdown file contains the pipeline from the PSM-level input data obtained from Proteome Discoverer. It provides an overview on structure and quality of the raw data (chunk 1-5), explores missing data structure and protein coverage across experiments (chunk 6-7), aggregates the psm-level data to proteins (chunk 8), and creates the linear model fits using Limma Bayes algorithms (chunk 10). The last two chunks (11+12) create the output data files and Volcano plots submitted with this manuscript.

References

Amos B, Aurrecoechea C, Barba M, Barreto A, Basenko EY, Bażant W, Belnap R, Blevins AS, Böhme U, Brestelli J, Brunk BP, Caddick M, Callan D, Campbell L, Christensen MB, Christophides GK, Crouch K, Davis K, DeBarry J, Doherty R, Duan Y, Dunn M, Falke D, Fisher S, Flicek P, Fox B, Gajria B, Giraldo-Calderón GI, Harb OS, Harper E, Hertz-Fowler C, Hickman MJ, Howington C, Hu S, Humphrey J, Iodice J, Jones A, Judkins J, Kelly SA, Kissinger JC, Kwon DK, Lamoureux K, Lawson D, Li W, Lies K, Lodha D, Long J, MacCallum RM, Maslen G, McDowell MA, Nabrzyski J, Roos DS, Rund SSC, Schulman SW, Shanmugasundram A, Sitnik V, Spruill D, Starns D, Stoeckert CJ, Tomko SS, Wang H, Warrenfeltz S, Wieck R, Wilkinson PA, Xu L, Zheng J. 2021. VEuPathDB: the eukaryotic pathogen, vector and host bioinformatics resource center. *Nucleic Acids Res* **50**:D898–D911. doi:10.1093/nar/gkab929

Anderson-White B, Beck JR, Chen C-T, Meissner M, Bradley PJ, Gubbels M-J. 2012. Chapter One Cytoskeleton Assembly in Toxoplasma gondii Cell Division In: Jeong KS, editor. International Review of Cell and Molecular Biology. pp. 1–31. doi:10.1016/b978-0-12-394309-5.00001-8

Anderson-White BR, Ivey FD, Cheng K, Szatanek T, Lorestani A, Beckers CJ, Ferguson DJP, Sahoo N, Gubbels M. 2011. A family of intermediate filament-like proteins is sequentially assembled into the cytoskeleton of Toxoplasma gondii. *Cell Microbiol* **13**:18–31. doi:10.1111/j.1462-5822.2010.01514.x

Aquilini E, Cova MM, Mageswaran SK, Pacheco NDS, Sparvoli D, Penarete-Vargas DM, Najm R, Graindorge A, Suarez C, Maynadier M, Berry-Sterkers L, Urbach S, Fahy PR, Guérin AN, Striepen B, Dubremetz J-F, Chang Y-W, Turkewitz AP, Lebrun M. 2021. An Alveolata secretory machinery adapted to parasite host cell invasion. *Nat Microbiol* **6**:425–434. doi:10.1038/s41564-020-00854-z

Barylyuk K, Koreny L, Ke H, Butterworth S, Crook OM, Lassadi I, Gupta V, Tromer E, Mourier T, Stevens TJ, Breckels LM, Pain A, Lilley KS, Waller RF. 2020. A Comprehensive Subcellular Atlas of the Toxoplasma Proteome via hyperLOPIT Provides Spatial Context for Protein Functions. *Cell Host & Microbe* **28**:752–766. doi:10.1016/j.chom.2020.09.011

860 Bisio H, Soldati-Favre D. 2019. Signaling cascades governing entry into and exit from host cells
861 by *Toxoplasma gondii*. *Annu Rev Microbiol* **73**:579–599. doi:10.1146/annurev-micro-020518-
862 120235

863 Carruthers VB, Sibley LD. 1997. Sequential protein secretion from three distinct organelles of
864 *Toxoplasma gondii* accompanies invasion of human fibroblasts. *European J Cell Biol* **73**:114–
865 123.

866 Chen AL, Kim EW, Toh JY, Vashisht AA, Rashoff AQ, Van C, Huang AS, Moon AS, Bell HN,
867 Bentolila LA, Wohlschlegel JA, Bradley PJ. 2015. Novel components of the *Toxoplasma* inner
868 membrane complex revealed by BioID. *mBio* **6**:e02357-14. doi:10.1128/mbio.02357-14

869 Cova MM, Lamarque MH, Lebrun M. 2022. How Apicomplexa parasites secrete and build their
870 invasion machinery. *Annu Rev Microbiol* **76**:619–640. doi:10.1146/annurev-micro-041320-
871 021425

872 Díaz-Martin RD, Rodriguez FES, Pozos SG, León CTG de, Castelán MM, Flores RM. 2022. A
873 comprehensive ultrastructural analysis of the *Toxoplasma gondii* cytoskeleton. *Parasitol Res*
874 **121**: 2065–2078. doi:10.1007/s00436-022-07534-3

875 Dubois DJ, Soldati-Favre D. 2019. Biogenesis and secretion of micronemes in *Toxoplasma*
876 *gondii*. *Cell Microbiol* **21**:e13018. doi:10.1111/cmi.13018

877 Dubremetz JF, Achbarou A, Bermudes D, Joiner KA. 1993. Kinetics and pattern of organelle
878 exocytosis during *Toxoplasma gondii* host-cell interaction. *Parasitology research* **79**:402–408.
879 doi:10.1007/bf00931830

880 Dubremetz JF, Torpier G. 1978. Freeze fracture study of the pellicle of an Eimerian sporozoite
881 (Protozoa, Coccidia). *J Ultra Mol Struct R* **62**:94–109. doi:10.1016/s0022-5320(78)90012-6

882 Engelberg K, Chen C-T, Bechtel T, Guzmán VS, Drozda AA, Chavan S, Weerapana E, Gubbels
883 M-J. 2020. The apical annuli of *Toxoplasma gondii* are composed of coiled-coil and signalling
884 proteins embedded in the inner membrane complex sutures. *Cellular Microbiology* **22**:e13112.
885 doi:10.1111/cmi.13112

886 Fu J, Zhao L, Yang J, Chen H, Cao S, Jia H. 2023. An unconventional SNARE complex
887 mediates exocytosis at the plasma membrane and vesicular fusion at the apical annuli in
888 *Toxoplasma gondii*. *Plos Pathog* **19**:e1011288. doi:10.1371/journal.ppat.1011288

889 Giuliano CJ, Wei KJ, Harling FM, Waldman BS, Farringer MA, Boydston EA, Lan TCT, Thomas
890 RW, Herneisen AL, Sanderlin AG, Coppens I, Dvorin JD, Lourido S. 2023. Functional profiling
891 of the *Toxoplasma* genome during acute mouse infection. *bioRxiv* 2023.03.05.531216.
892 doi:10.1101/2023.03.05.531216

893 Gould SB, Tham W-H, Cowman AF, McFadden GI, Waller RF. 2008. Alveolins, a new family of
894 cortical proteins that define the protist infrakingdom Alveolata. *Mol Biol Evol* **25**:1219–1230.
895 doi:10.1093/molbev/msn070

896 Gras S, JIMÉNEZ-RUIZ E, Klinger CM, Schneider K, Klingl A, Lemgruber L, Meissner M. 2019.
897 An endocytic-secretory cycle participates in *Toxoplasma gondii* in motility. *PLoS Biology*
898 **17**:e3000060. doi:10.1371/journal.pbio.3000060

899 Griffith MB, Pearce CS, Heaslip AT. 2022. Dense granule biogenesis, secretion, and function in
900 *Toxoplasma gondii*. *J Eukaryot Microbiol* **69**:e12904. doi:10.1111/jeu.12904

901 Gubbels M-J, Coppens I, Zarringhalam K, Duraisingh MT, Engelberg K. 2021. The modular
902 circuitry of apicomplexan cell division plasticity. *Front Cell Infect Microbiol* **11**:670049.
903 doi:10.3389/fcimb.2021.670049

904 Guérin A, Strelau KM, Barylyuk K, Wallbank BA, Berry L, Crook OM, Lilley KS, Waller RF,
905 Striepen B. 2023. *Cryptosporidium* uses multiple distinct secretory organelles to interact with
906 and modify its host cell. *Cell Host Microbe* **31**: 650-664 doi:10.1016/j.chom.2023.03.001

907 Guindon S, Dufayard J-F, Lefort V, Anisimova M, Hordijk W, Gascuel O. 2010. New algorithms
908 and methods to estimate maximum-likelihood phylogenies: assessing the performance of
909 PhyML 3.0. *Syst Biol* **59**:307–321. doi:10.1093/sysbio/syq010

910 Gyimesi G, Hediger MA. 2022. Systematic in silico discovery of novel solute carrier-like proteins
911 from proteomes. *PLoS ONE* **17**:e0271062. doi:10.1371/journal.pone.0271062

912 Hakimi M-A, Olias P, Sibley LD. 2017. *Toxoplasma* effectors targeting host signaling and
913 transcription. *Clinical Microbiology Reviews* **30**:615–645. doi:10.1128/cmr.00005-17

914 Hallgren J, Tsirigos KD, Pedersen MD, Armenteros JJA, Marcatili P, Nielsen H, Krogh A, Winther
915 O. 2022. DeepTMHMM predicts alpha and beta transmembrane proteins using deep neural
916 networks. doi:10.1101/2022.04.08.487609

917 Havelaar AH, Kirk MD, Torgerson PR, Gibb HJ, Hald T, Lake RJ, Praet N, Bellinger DC, Silva
918 NR de, Gargouri N, Speybroeck N, Cawthorne A, Mathers C, Stein C, Angulo FJ,
919 Devleesschauwer B, Group WHOFDBER. 2015. World Health Organization global estimates
920 and regional comparisons of the burden of foodborne disease in 2010. *PLOS Med*
921 **12**:e1001923. doi:10.1371/journal.pmed.1001923

922 Heaslip AT, Nelson SR, Warshaw DM. 2016. Dense granule trafficking in *Toxoplasma gondii*
923 requires a unique class 27 myosin and actin filaments. *Mol Biol Cell* **27**:2080–2089.
924 doi:10.1091/mbc.e15-12-0824

925 Hu K, Johnson J, Florens L, Fraunholz M, Suravajjala S, DiLullo C, Yates J, Roos DS, Murray
926 JM. 2006. Cytoskeletal components of an invasion machine--the apical complex of
927 *Toxoplasma gondii*. *PLOS Pathog* **2**:e13. doi:10.1371/journal.ppat.0020013

928 Jahn R, Scheller RH. 2006. SNAREs — engines for membrane fusion. *Nat Rev Mol Cell Biol*
929 **7**:631–643. doi:10.1038/nrm2002

930 Jia Y, Marq J-B, Bisio H, Jacot D, Mueller C, Yu L, Choudhary J, Brochet M, Soldati-Favre D.
931 2017. Crosstalk between PKA and PKG controls pH-dependent host cell egress of
932 *Toxoplasma gondii*. *EMBO Journal* **36**:3250–3267. doi:10.15252/embj.201796794

933 Katoh K, Standley DM. 2013. MAFFT multiple sequence alignment software version 7:
934 improvements in performance and usability. *Molecular Biology and Evolution* **30**:772–780.
935 doi:10.1093/molbev/mst010

936 Katris NJ, Ke H, McFadden GI, Dooren GG van, Waller RF. 2019. Calcium negatively regulates
937 secretion from dense granules in *Toxoplasma gondii*. *Cellular Microbiology* e13011.
938 doi:10.1111/cmi.13011

939 Kelsey JS, Fastman NM, Blumberg DD. 2012. Evidence of an evolutionarily conserved lmbr1
940 domain-containing protein that associates with endocytic cups and plays a role in cell
941 migration in *Dictyostelium discoideum*. *Eukaryot Cell* **11**:401–416. doi:10.1128/ec.05186-11

942 Klinger CM, Jimenez-Ruiz E, Mourier T, Klingl A, Lemgruber L, Pain A, Dacks JB, Meissner M.
943 2022. Evolution of lineage-specific trafficking proteins and a novel post-Golgi trafficking
944 pathway in Apicomplexa. *bioRxiv* 2022.12.12.520010. doi:10.1101/2022.12.12.520010

945 Koike S, Jahn R. 2022. SNARE proteins: zip codes in vesicle targeting? *Biochem J* **479**:273–
946 288. doi:10.1042/bcj20210719

947 Koreny L, Mercado-Saavedra BN, Klinger CM, Barylyuk K, Butterworth S, Hirst J, Rivera-Cuevas
948 Y, Zaccai NR, Holzer VJC, Klingl A, Dacks JB, Carruthers VB, Robinson MS, Gras S, Waller
949 RF. 2023. Stable endocytic structures navigate the complex pellicle of apicomplexan
950 parasites. *Nat Commun* **14**:2167. doi:10.1038/s41467-023-37431-x

951 Koreny L, Zeeshan M, Barylyuk K, Tromer EC, Hooff JJE van, Brady D, Ke H, Chelaghma S,
952 Ferguson DJP, Eme L, Tewari R, Waller RF. 2021. Molecular characterization of the conoid
953 complex in *Toxoplasma* reveals its conservation in all apicomplexans, including Plasmodium
954 species. *PLoS Biol* **19**:e3001081. doi:10.1371/journal.pbio.3001081

955 Lebrun M, Carruthers VB, Cesbron-Delauw M-F. 2014. *Toxoplasma* secretory proteins and their
956 roles in cell invasion and intracellular survival In: Weiss LM, Kim K, editors. *Toxoplasma*
957 *Gondii* The Model Apicomplexan. pp. 389–453. doi:10.1016/b978-0-12-396481-6.00012-x

958 Lentini G, Dubois DJ, Maco B, Soldati-Favre D, Frénal K. 2019. The roles of Centrin 2 and
959 Dynein Light Chain 8a in apical secretory organelles discharge of *Toxoplasma gondii*. *Traffic*
960 **20**:583–600. doi:10.1111/tra.12673

961 Leung JM, Liu J, Wetzel LA, Hu K. 2019. Centrin2 from the human parasite *Toxoplasma gondii* is
962 required for its invasion and intracellular replication. *J Cell Sci* **132**:jcs228791.
963 doi:10.1242/jcs.228791

964 MacGregor P, Nene V, Nisbet RER. 2021. Tackling protozoan parasites of cattle in sub-Saharan
965 Africa. *PLoS Pathog* **17**:e1009955. doi:10.1371/journal.ppat.1009955

966 Montoya JG, Liesenfeld O. 2004. Toxoplasmosis. *Lancet* **363**:1965–1976. doi:10.1016/s0140-
967 6736(04)16412-x

968 Neveu E, Khalifeh D, Salamin N, Fasshauer D. 2020. Prototypic SNARE proteins are encoded in
969 the genomes of Heimdallarchaeota, potentially bridging the gap between the prokaryotes and
970 eukaryotes. *Curr Biol* **30**: 2468-2480

971 Pacheco ND, Vetterling JM, Doran DJ. 1975. Ultrastructure of cytoplasmic and nuclear changes
972 in *Eimeria tenella* during first-generation schizogony in cell culture. *J Parasitol* **61**:31–42.

973 Pacheco NDS, Tosetti N, Koreny L, Waller RF, Soldati-Favre D. 2020. Evolution, composition,
974 assembly, and function of the conoid in Apicomplexa. *Trends Parasitol* **36**:688–704.
975 doi:10.1016/j.pt.2020.05.001

976 Perez-Riverol Y, Bai J, Bandla C, García-Seisdedos D, Hewapathirana S, Kamatchinathan S,
977 Kundu DJ, Prakash A, Frericks-Zipper A, Eisenacher M, Walzer M, Wang S, Brazma A,
978 Vizcaíno JA. 2021. The PRIDE database resources in 2022: a hub for mass spectrometry-
979 based proteomics evidences. *Nucleic Acids Res* **50**:D543–D552. doi:10.1093/nar/gkab1038

980 Redl B, Habeler M. 2022. The diversity of lipocalin receptors. *Biochimie* **192**:22–29.
981 doi:10.1016/j.biochi.2021.09.008

982 Ritchie ME, Phipson B, Wu D, Hu Y, Law CW, Shi W, Smyth GK. 2015. limma powers differential
983 expression analyses for RNA-sequencing and microarray studies. *Nucleic Acids Res* **43**:e47–
984 e47. doi:10.1093/nar/gkv007

985 Roiko MS, Svezhova N, Carruthers VB. 2014. Acidification activates *Toxoplasma gondii* motility
986 and egress by enhancing protein secretion and cytolytic activity. *PLOS Pathogens*
987 **10**:e1004488. doi:10.1371/journal.ppat.1004488

988 Roos DS, Donald R, Morrissette NS, Moulton ALC. 1994. Molecular tools for genetic dissection
989 of the protozoan parasite *Toxoplasma gondii*. Methods in Cell Biology. Adacemic Press. pp.
990 27–63. doi:10.1016/s0091-679x(08)61845-2

991 Sheffield HG, Melton ML. 1968. The fine structure and reproduction of *Toxoplasma gondii*. *J*
992 *Parasitol.* **54**:209–226.

993 Sheiner L, Demerly JL, Poulsen N, Beatty WL, Lucas O, Behnke MS, White MW, Striepen B.
994 2011. A systematic screen to discover and analyze apicoplast proteins identifies a conserved
995 and essential protein import factor. *PLOS Pathog* **7**:e1002392.

996 Striepen B. 2013. Parasitic infections: Time to tackle cryptosporidiosis. *Nature* **503**:189–191.

997 Striepen B, Jordan CN, Reiff S, Dooren GG van. 2007. Building the perfect parasite: cell division
998 in apicomplexa. *PLOS Pathog* **3**:e78. doi:10.1371/journal.ppat.0030078

999 Suarez C, Lentini G, Ramaswamy R, Maynadier M, Aquilini E, Berry-Sterkers L, Cipriano M,
1000 Chen AL, Bradley P, Striepen B, Boulanger MJ, Lebrun M. 2019. A lipid-binding protein
1001 mediates rhoptry discharge and invasion in *Plasmodium falciparum* and *Toxoplasma gondii*
1002 parasites. *Nature communications* **10**:4041. doi:10.1038/s41467-019-11979-z

1003 Suvorova ES, Francia M, Striepen B, White MW. 2015. A novel bipartite centrosome coordinates
1004 the apicomplexan cell cycle. *PLoS Biology* **13**:e1002093. doi:10.1371/journal.pbio.1002093

1005 The M, MacCoss MJ, Noble WS, Käll L. 2016. Fast and accurate protein false discovery rates on
1006 large-scale proteomics data sets with percolator 3.0. *J Am Soc Mass Spectrom* **27**:1719–
1007 1727. doi:10.1007/s13361-016-1460-7

1008 Uboldi AD, Wilde M-L, McRae EA, Stewart RJ, Dagley LF, Yang L, Katris NJ, Hapuarachchi SV,
1009 Coffey MJ, Lehane AM, Botté CY, Waller RF, Webb AI, McConville MJ, Tonkin CJ. 2018.
1010 Protein kinase A negatively regulates Ca2+ signalling in *Toxoplasma gondii*. *PLoS Biology*
1011 **16**:e2005642-32. doi:10.1371/journal.pbio.2005642

1012 Venugopal K, Chehade S, Werkmeister E, Barois N, Periz J, Lafont F, Tardieux I, Khalife J,
1013 Langsley G, Meissner M, Marion S. 2020. Rab11A regulates dense granule transport and
1014 secretion during *Toxoplasma gondii* invasion of host cells and parasite replication. *PLoS*
1015 *Pathog* **16**:e1008106. doi:10.1371/journal.ppat.1008106

1016 Wan W, Dong H, Lai D-H, Yang J, He K, Tang X, Liu Q, Hide G, Zhu X-Q, Sibley LD, Lun Z-R,
1017 Long S. 2023. The *Toxoplasma* micropore mediates endocytosis for selective nutrient salvage
1018 from host cell compartments. *Nat Commun* **14**:977. doi:10.1038/s41467-023-36571-4

1019 WHO. 2021. World malaria report 2021. Geneva: World Health Organisation.

1020